Rybacki, E., Janssen, C., Wirth, R., Chen, K., Wenk, H.-R., Stromeyer, D., Dresen, G. (2011): Low-temperature deformation in calcite veins of SAFOD core samples (San Andreas Fault) - Microstructural analysis and implications for fault rheology. - Tectonophysics, 509, 1-2, 107-119

DOI: 10.1016/j.tecto.2011.05.014

Tectonophysics 509 (2011) 107-119

Low-temperature deformation in calcite veins of SAFOD core samples (San Andreas Fault) — Microstructural analysis and implications for fault rheology

E. Rybacki[a,*], C. Janssen[a], R. Wirth[a], K. Chen[b], H.-R. Wenk[b], D. Stromeyer[a], G. Dresen[a]

[a] GFZ German Research Centre for Geosciences, Telegrafenberg, 14473 Potsdam, Germany
[b] Department of Earth and Planetary Science, University of California, Berkeley, CA, United States

ARTICLE INFO

Article history:
Received 2 November 2010
Received in revised form 30 May 2011
Accepted 31 May 2011
Available online 15 June 2011

Keywords:
SAFOD
Calcite
Microstructure
Stress
Piezometer
Residual strain

ABSTRACT

The microstructures of four core samples from the San Andreas Fault Observatory at Depth (SAFOD) were investigated with optical and transmission electron microscopy. These samples, consisting of sandstone, siltstone, and fault gouge from phase III of the drilling campaign (3141–3307 m MD), show a complex composition of quartz, feldspar, clays, and amorphous material. Microstructures indicate intense shearing and dissolution–precipitation as main deformation processes. The samples also contain abundant veins filled with calcite. Within the inspected veins the calcite grains exhibit different degrees of deformation with evidence for twinning and crystal plasticity. Dislocation densities (ranging from ≈ $3\cdot10^{12}$ m^{-2} to ≈ $3\cdot10^{13}$ m^{-2}) and twin line densities (≈22 mm^{-1} – 165 mm^{-1}) are used as paleo-piezometers. The corresponding estimates of differential stresses vary between 33 and 132 MPa, deduced from dislocation density and 92-251 MPa obtained from twin density, possibly reflecting chronologically different maximum stress states and/or grain scale stress perturbations. Mean values of stress estimates are 68 ±46 MPa and 168 ± 60 MPa, respectively, where estimates from dislocation density may represent a lower bound and those from twin density an upper bound. The stress estimates are also compatible with residual lattice strains determined with microfocus Laue diffraction yielding equivalent stresses of 50–300 MPa in twinned calcite. The lower stress bound agrees with stress estimates from borehole breakout measurements performed in the pilot hole. From these data and assuming hydrostatic pore pressure and a low intermediate principal stress close to the overburden stress, frictional sliding of the San Andreas Fault at the SAFOD site is constrained to friction coefficients between 0.24 and 0.31. These low friction values may be related to the presence of clays, talc, and amorphous phases found in the fault cores and support the hypothesis of a weak San Andreas Fault.

1. Introduction

Numerous geological and geophysical studies investigate the rheological/mechanical behavior of faults with respect to earthquake nucleation and the role of fluids in fault weakening (e.g., *Brodsky et al.*, 2010; *Chester and Logan*, 1986; *Evans and Chester*, 1995; *Fagereng et al.*, 2010; *Fulton et al.*, 2009; *Schulz and Evans*, 2000). In this context, fault-related veins play a key role in understanding faulting processes and the analysis of veins has emerged as a useful tool to study the behavior of faults. The composition of veins and their deformation mechanisms may provide information about fluid sources, fluid circulation, pressure and temperature-conditions, chemical alteration processes and fault rheology in general (*Gratier et al.*, 2003; *Herwegh et al.*, 2005; *Herwegh and Kunze*, 2002; *Janssen et al.*, 1998). In addition, the formation of syntectonic veins may indicate elevated fluid pressure during vein formation because local high fluid pressures are often required to open fractures (*Mittempergher et al.*, 2011; *Pollard and Segall*, 1987; *Wiltschko et al.*, 2009). The state of stress of the San Andreas Fault (SAF) has long been a matter of debate. Some authors have suggested the fault to be mechanically weak (e.g., *Brune et al.*, 1969; *Lachenbruch and Sass*, 1980, 1992; *Lockner et al.*, 2011; *Townend and Zoback*, 2004; *Zoback et al.*, 1987) whereas others advocated for a strong fault (e.g., *Scholz*, 2000; *Scholz and Hanks*, 2004). It is assumed that a weak fault with a low friction coefficient (≤ 0.2) may be due to the presence of high pore pressures and/or serpentinite, talc, or clay minerals. Reducing stresses in the upper crust to a few tens of MPa is also required to explain the lack of increased heat flow along the trace of the SAF (e.g., *Carpenter et al.*, 2009; *Chéry et al.*, 2004; *Collettini et al.*, 2009; *Lachenbruch and Sass*, 1980; *Moore and Rymer*, 2007; *Tembe et al.*, 2009). For rocks with a friction coefficient ≥ 0.6, in accordance with laboratory results (*Byerlee*, 1978), stresses at depth will exceed 100 MPa for an optimally oriented fault with respect to the direction of the maximum principal stress, requiring a reorientation of the maximum principal stress close to the fault towards a more acute angle with the SAF than what is measured in the far field. A combination of low friction minerals, local overpressure and/or local stress variations may also hold at the SAF (e.g., *Faulkner et al.*, 2006; *Hardebeck and Michael*, 2004).

Hickman and Zoback (2004) estimated the stress orientation and magnitude in the SAFOD pilot hole near Parkfield, California, down to about 2 km depth. The authors infer low differential stresses of about 60-70 MPa operating in the fault zone at ≈ 2.2 km depth based on borehole breakout data, but considerable uncertainties exist. Here, we present a detailed microstructure analysis of calcite veins within samples from the SAFOD main borehole. First, we describe microstructures examined with optical and transmission electron microscopes (TEM) with the aim of providing information on fault evolution. Second, we interpret dislocation and twin densities measured in the calcite veins to arrive at stress estimates based on paleo-piezometric relationships. Finally we compare microscopic observations with lattice strain measurements on the same samples with synchrotron microfocus Laue diffraction.

2. Geological setting of the San Andreas Fault

Central California is geologically separated by the San Andreas Fault (SAF), which is a transform fault at the boundary between the western Pacific plate and the eastern North American Plate. The SAFOD drill site is located at the transition between the creeping Parkfield segment in the North and the

* Corresponding author.
E-mail address: uddi@gfz-potsdam.de (E. Rybacki).

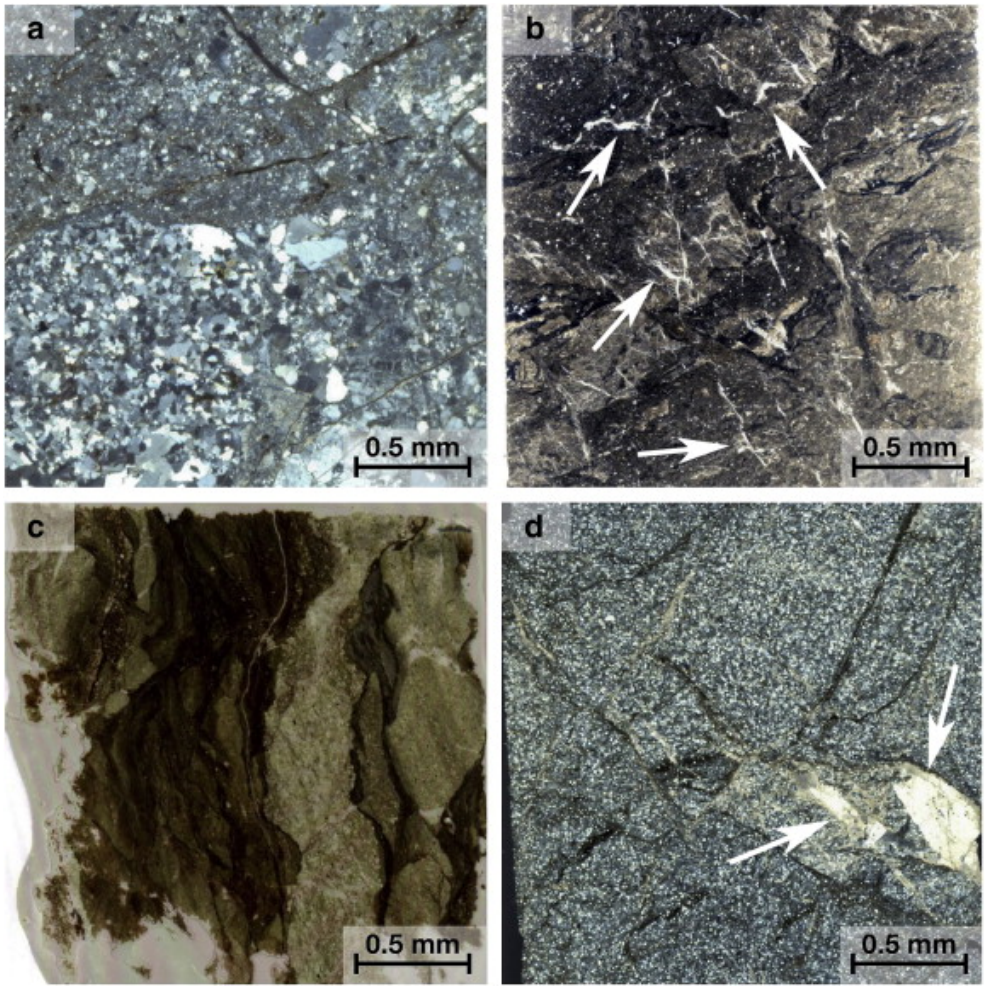

Figure 1. Low magnification photographs of thin sections from samples S1–S4. (a) Angular quartz and feldspar grains (fragments) in a sandy matrix. (b) Gouge composed of very fine-grained matrix of quartz and clay (grain size < 1 μm). The matrix is fractured with calcite filling (arrows). (c) Dark-brown fractured and fine-grained scaly clay matrix with dark pressure solution seams. (d) Quartz and feldspar grains lie in a matrix of highly comminuted clay. Arrows point to few larger calcite grains.

locked segment of the SAF to the South. Near the drill site arkosic sedimentary rocks predominate at the southwest of the fault and Great Valley sedimentary rocks northeast of the fault (*Springer et al.*, 2009). Within the SAFOD drill holes four major geological units have been identified (*Bradbury et al.*, 2007) with Quaternary and Tertiary sediments, Salinian granite and arkosic sediments beneath the Buzzard Canyon fault. Approximately 1200 m NE of the drill site the arkosic sediments of the Salinian terrane (Pacific plate) are replaced by claystones and siltstones of the Great Valley/Franciscan terrane (North American plate), which may represent an ancestral trace of the SAF. The wellbore crosscuts several active fault strands as for example at depths of 3194 m and 3301 m. Creeping fault segments are revealed by pronounced and ongoing casing deformation (*Bradbury et al.*, 2007; *Zoback et al.*, 2010).

3. Description of samples

We analyzed the microstructures of four samples (S1-4) obtained from SAFOD phase III cores (for a detailed description of cores see also Photographic Atlas of the SAFOD Phase 3 Cores 2007, URL http://www.earthscope.org/data/safod_core_viewer). The samples, which are described in detail by *Janssen et al.* (2010, 2011), were recovered from different core sections located close to or at small distance to the zones of active deformation. Sample S1 is from the arkosic sedimentary rock sequence and samples S2–S4 are from the Great Valley sequence.

Sample S1 was taken from a fractured, grayish-red to brownish sandstone (hole E, run 1, section 6, 3141 m (10,322 ft) MD, depth in m refers to Phase 2 Baker-Atlas open hole log, cf. *Zoback et al.*, 2010, and (uncorrected) depth in feet to the core viewer atlas, see url given above), close to a fault-contact between silt- and sandstone. The matrix (Fig. 1a) contains coarse subrounded grains of feldspar (22 vol.% plagioclase, 17 vol.% microcline, 4 vol.% orthoclase), 36 vol.% quartz, and 21 vol.% laumonite, as determined by X-ray diffraction analysis. Some grains are intersected by thin (< 200 μm) calcite veins.

Sample S2 was collected at 3189 m (10,449 ft) MD (hole G, run 2, section 4). This core section is close to the section of active casing deformation, representing the southwest deforming zone (SDZ) of the SAF at a measured depth of 3191–3193 m. The strongly foliated gouge contains about 50 vol.% quartz, 22 vol.% clay (illite/smectite) with a grain size < 1 μm, and 13 vol.% feldspar clasts. Several calcite vein generations (5 vol.%) are present (Fig. 1b). The youngest veins overprint a fault-related fabric, which contains about 9 vol.% of amorphous material (*Janssen et al.*, 2010). Preferred orientation of grains, pressure solution seams and authigenic clay minerals indicate pervasive shearing and dissolution–precipitation processes, respectively (see also *Hickman et al.*, 2008; *Gratier et al.*, 2009; *Schleicher et al.*, 2009).

Sample S3 was prepared from hole G, run 4, section 2 (3300 m, 10,813.4 ft MD), which is very close to the active central deformation zone (CDZ) at 3300-3303 m MD. The sample shows a polished slip surface with slickensides. Mineral content

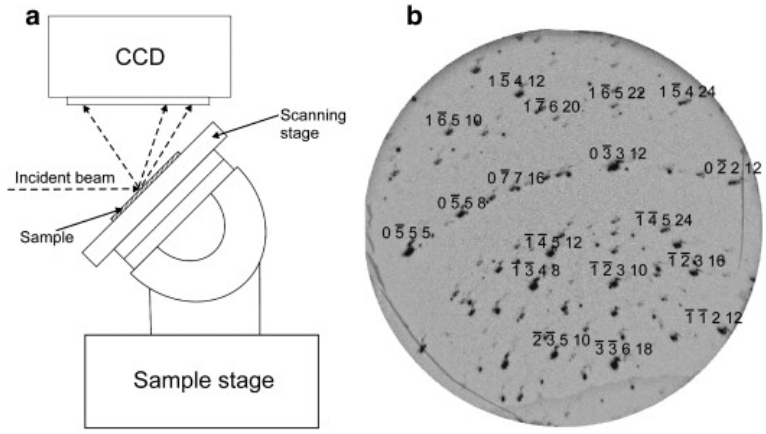

Figure 2. (a) Schematic drawing of the X-ray microdiffraction experimental configuration in reflection mode with incident X-ray beam, sample slab and CCD detector centered at 90° to the incident beam. (b) Laue diffraction patterns of SAFOD calcite with the Miller indices for some of the diffraction peaks. Note the distortion of lattice spots due to plastic deformation.

is 38 vol.% illite–smectite (I–S), 12 vol.% chlorite, 30 vol.% quartz, and 10 vol.% plagioclase, forming a fine-grained scaly matrix (Fig. 1c) with a minor content of calcite (3 vol.%), hematite (3 vol.%), and amorphous material (4 vol.%). Calcite occurs as veinlets between fractured grains. Authigenic clay minerals and pressure solution relicts suggest activity of dissolution-precipitation processes.

Sample S4 was taken from fractured massive siltstones at a depth of 3307 m (10,837.5 ft, hole G, run 5, section 4). The sample contains a mixture of numerous subangular matrix blocks and microbreccias, partly displaying a scaly fabric (Fig. 1d). Major mineral constituents are illite/smectite (47 vol.%), quartz (26 vol.%), plagioclase (22 vol.%), and analcime (5 vol.%).

4. Analytical techniques

In this study we focus on the microstructures of the calcite veins contained in the 4 samples investigated. We quantify density of calcite twins and the density of dislocations within the calcite grains to arrive at an estimate of the paleo-stresses governing deformation of the gouge during and after vein formation. In addition, stresses are estimated using residual strain analysis.

4.1. Calcite twinning

The density of twins was measured using an optical microscope (Leica DM RX) with an attached high-resolution digital camera (Leica DFC 420). Measurements were performed on polished thin sections. To determine the twin density, the number of twins perpendicular to the twin boundaries of individual grains was counted and normalized to a unit length of 1 mm. For grains containing multiple twin sets we applied this procedure on each orientation and calculated the average value. We measured the twin (line-) density of calcite grains within veins at 7 different positions in the 4 samples. Average densities given below are calculated from 6 to 58 individual measurements at each position. We restricted the measurement of twin densities to twins visible by optical microscopy (≥ 1 μm) for application of the associated piezometer (see below). It should be noted, however, that deformed carbonates also contain (mainly secondary) thin twins with a width below the limit of optical resolution (*Barber and Wenk*, 1979), which appear to correlate with the deformation conditions (*Ebert et al.*, 2007).

4.2. Dislocation microstructures

Transmission electron microcopy was performed using a FEI Tecnai G2 F20 X-Twin transmission electron microscope (TEM/AEM) including a Fishione high-angle annular dark field detector (HAADF). For the analysis, thin (0.15 μm) foils of about 10 × 5 μm in size were prepared with the focused ion beam (FEI FIB200TEM) technique (*Wirth*, 2004, 2009). For determination of dislocation densities, defined as the total length of dislocation lines per unit volume, we used two different techniques, assuming a random orientation of the dislocations with respect to the foil plane. First, a grid of lines was projected on each micrograph. The average dislocation density ρ_{disloc} was calculated using the relation $\rho_{disloc} = 2 \cdot n/(L \cdot d)$, where n is the number of intersections of dislocation lines with the grid lines of total length L, and d is thickness of the FIB-foil (line intercept method, e.g. *Ham*, 1961; *Pezzotti and Kleebe*, 1996; *De Bresser*, 1996).

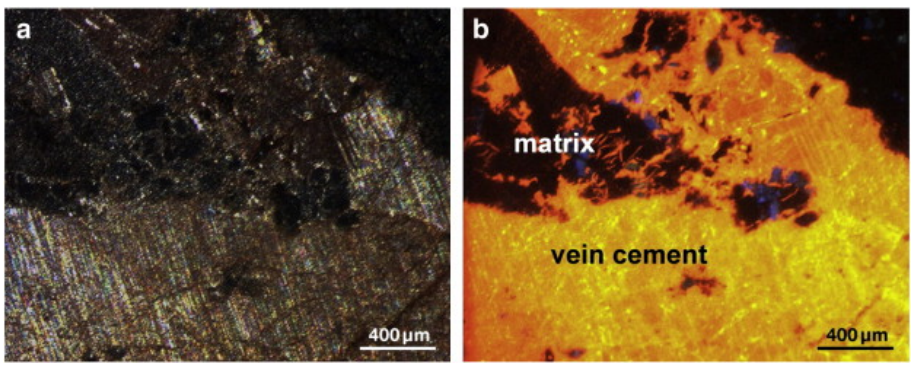

Figure 3. Photomicrograph of microstructures with crossed polarizers (a) and CL-photograph (b) of the same region. Contact area between matrix and vein cement. Note that the calcite vein shows uniform yellow to orange CL-colors and that the matrix is not luminescent.

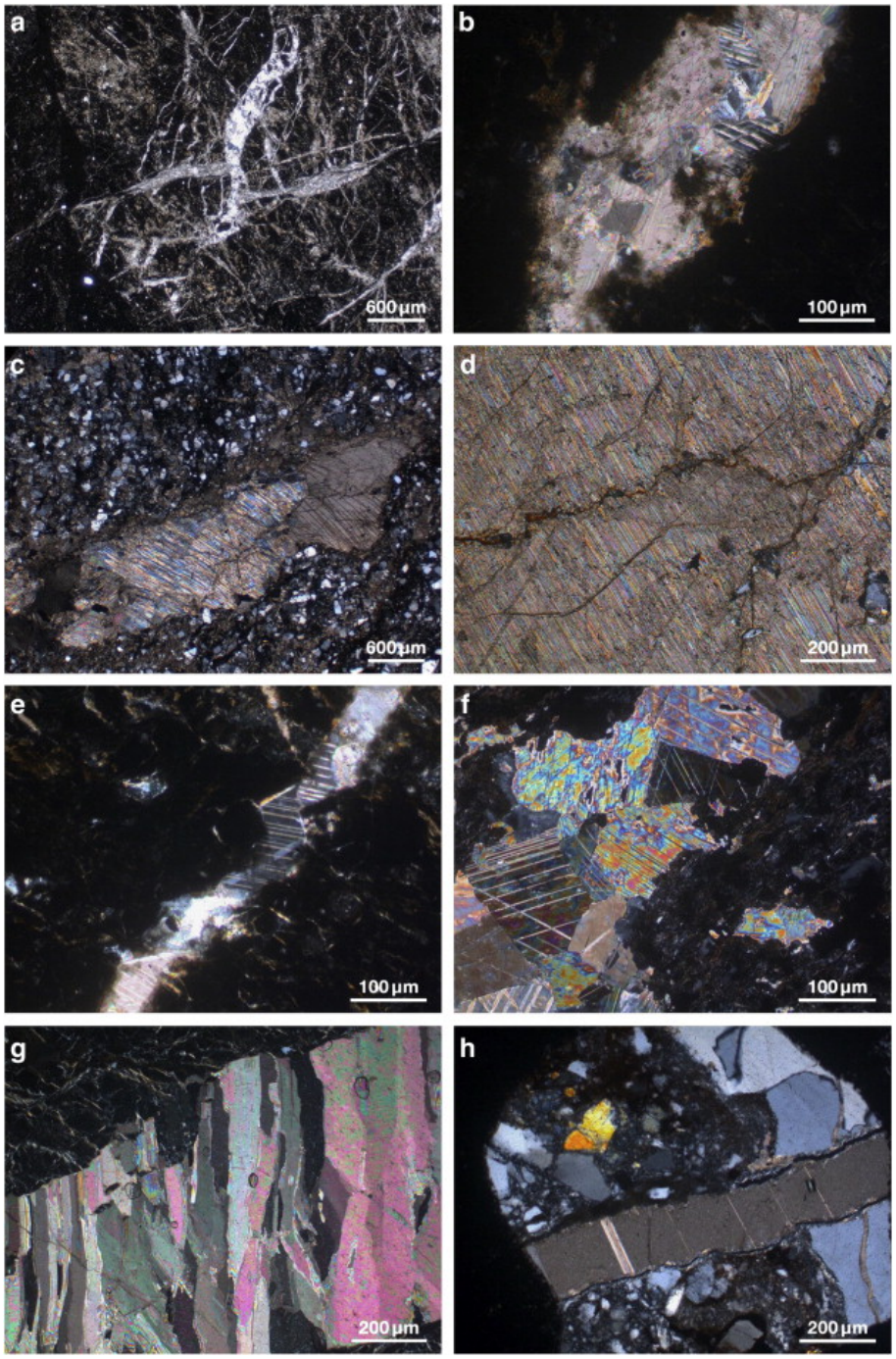

Figure 4. Photomicrographs of calcite veins in the SAFOD samples with crossed polarizers. a) Heavily veined and fractured gouge sample. b) Calcite vein in mudstone filled by coarse twinned calcite cement. c) Calcite vein/patch within siltstone matrix. Dark pressure solution seams marking the boundary between vein and matrix. d) Twinned vein cement with straight twins, dissected by stylolitic seams. e) Moderately deformed thin calcite vein. f) Calcite patches with intersecting deformation twins. g) Fibrous calcite crystals are not twinned and not fractured indicating that healing processes outlasted the period of brittle faulting. h) Calcite vein with only few twinned grains, dominantly by a twin set with straight and thin twin lamellae.

Secondly, we applied the foil intercept method (*Ham and Sharpe*, 1961; *Schoek*, 1961), where the dislocation density is determined from the number N of intersection of dislocations with the two surfaces of a foil of cross-section A, which gives $\rho_{disloc} = 2\,N/A$. Comparison of the two methods reveals that the second method yields a dislocation density, which is in average ≈ 20% higher than determined by the first approach. In the following, we report the densities measured by the line intercept method since *De Bresser* (1996) also used this method for experimental calibration of a calcite paleo-piezometer. Measurements were performed on 23 representative images from 4 different foils of samples S1, S2 and S4, each covering an area between ≈ 1 and 11 µm². Counting was restricted to areas with more or less free dislocations trying to avoid regions with dislocation tangles for example associated with twin boundaries.

4.3. Residual strain

Microstructures, including deformation twinning, orientation, and residual strain/stress distribution, of calcite in sample S2 were also studied using synchrotron polychromatic X-ray Laue microdiffraction on Beamline 12.3.2 at the Advanced Light Source (ALS) of Lawrence Berkeley National Laboratory (LBNL) to investigate residual stress (*Kunz et al.*,2009). The energy

Table 1
Results of SAFOD phase III samples' microstructural analysis.

Sample	Depth m		$\rho_{dislocations}$ m^{-2}	ρ_{twins} mm^{-1}	$\Delta\sigma_{disloc}$ MPa	$\Delta\sigma_{twin}$ MPa	$\Delta\sigma_{resls}$ MPa
S1c	2593	Range	$2.2\cdot10^{12}$–$3.3\cdot10^{12}$	10–63	28–36	62–155	
		Average	$\mathbf{(2.9 \pm 1.1)\cdot10^{12}}$	**27 ± 14**	**33 ± 7**	**101 ± 27**	
S2a	2619	Range	$1.4\cdot10^{13}$–$4.5\cdot10^{13}$	82–182	87–180	177–263	50–300
		Average	$\mathbf{(2.7 \pm 1.3)\cdot10^{13}}$	**135 ± 41**	**132 ± 39**	**226 ± 35**	**140–190**
S2a	2619	Range		14–113		73–207	
		Average		**56 ± 40**		**145 ± 52**	
S2a	2619	Range	$2.2\cdot10^{12}$–$4.4\cdot10^{12}$	0–65	28–43	0–157	
		Average	$\mathbf{(3.2 \pm 1.3)\cdot10^{12}}$	**22 ± 21**	**35 ± 7**	**92 ± 42**	
S3a	2674	Range		11–188		65–267	
		Average		**93 ± 37**		**188 ± 38**	
S4a	2678	Range	$0.5\cdot10^{13}$–$1.6\cdot10^{13}$	210–277	46–95	214–325	
		Average	$\mathbf{(1.1 \pm 0.5)\cdot10^{13}}$	**165 ± 57**	**74 ± 20**	**251 ± 43**	
S4c	2678	Range		47–107		134–202	
		Average		**80 ± 27**		**175 ± 29**	

$\rho_{dislocations}$ is dislocation density and ρ_{twins} is twin line density of calcite veins. Resulting differential stress estimates $\Delta\sigma_{disloc}$ and $\Delta\sigma_{twin}$ were calculated using paleo–piezometers and $\Delta\sigma_{resls}$ from analysis of the residual lattice strain. Depth is given as vertical depth below ground level.

range of the X-ray beam on this beamline was 5 to 24 keV. The X-ray beam size was focused to about 1 μm² at the focal point using a pair of Kirkpatrick–Baez (KB) mirrors. The thin sectioned sample was mounted on the sample stage and tilted 45° with respect to the incident beam (Fig. 2a). A 70 μm × 70 μm area was scanned with 1 μm step size and 0.5 s exposure time. A Laue diffraction pattern was produced at each position where the focused X-ray beam interacted with calcite crystal. A 133 mm diameter 2D MAR133 X-ray CCD detector was mounted 8 cm above the sample and 90° with respect to the incident beam and recorded Laue diffraction patterns. An example is shown in Fig. 2b. All 4900 Laue diffraction patterns were automatically indexed with rhombohedral lattice parameters ($a = b = c = 6.375$ Å, $\alpha = \beta = \gamma = 46.076°$; *Graf*, 1961) using a custom developed software package XMAS (*Tamura et al.*, 2009) and then converted to a hexagonal lattice to obtain the information of orientation and strain tensor at each scanning spot. More detailed information about strain analysis in calcite is reported elsewhere (*Chen et al.*, 2011).

5. Microstructures

5.1. Microscopic description of calcite veins and twin densities

Veins within the four SAFOD core samples are composed of

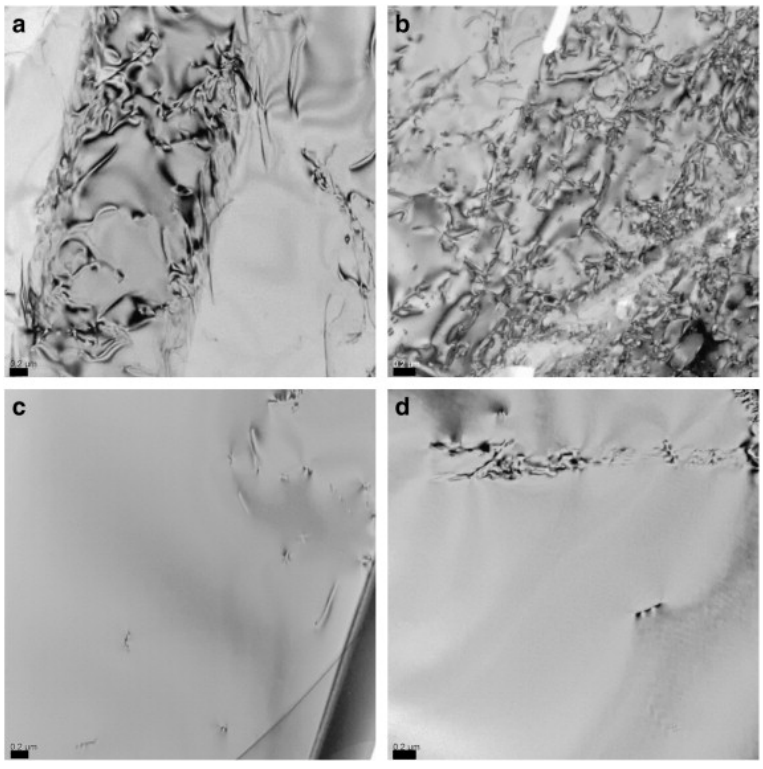

Figure 5. TEM micrographs of calcite in veins showing examples of strongly deformed grains with high dislocation density in sample S4a (a) and sample S2a (b) and of weakly deformed calcite in sample S1c (c) and sample S2a (d). Scale bar is 0.2 μm.

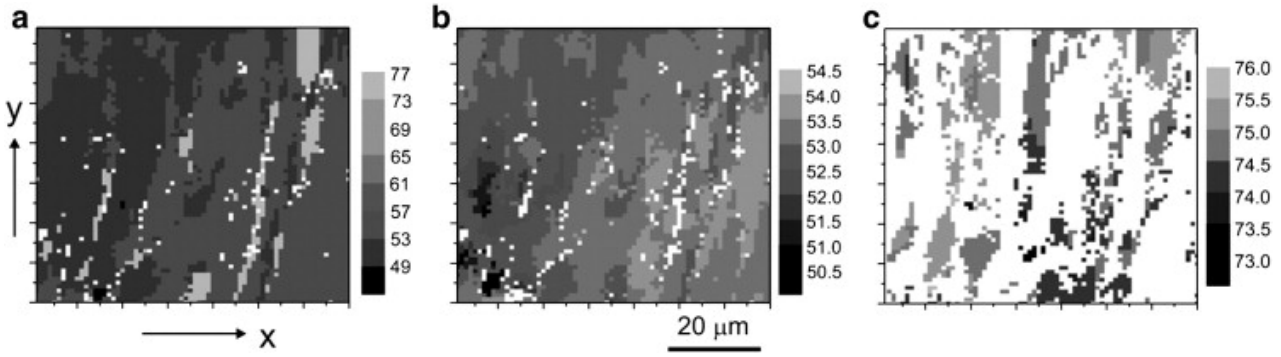

Figure 6. Orientation maps showing the angles between crystal *c*-axis and sample *z*-axis (perpendicular to the sample surface) obtained from microfocus Laue patterns. (a) Crystal domain that diffracts the strongest at each scan position, (b) host domain, and (c) the twin domain. The sample coordinate system x, y, z refers to the thin section.

calcite. Density of calcite veins progressively increases toward the active fault trace suggesting that the veins formed during or after faulting. Using the cathodoluminescence (CL)-microscope reveals uniform yellow to orange CL-colors for all calcite veins (Fig. 3). The homogeneous CL pattern in the vein cements corroborate the lack of fluid pulses into the fault rocks, since with every fluid pulse (for example meteoric water) the chemistry of the fluid would slightly change owing to differences in the solute concentration. We observed no zoning of crystals possibly indicating fast precipitation of vein calcites (*Gratier and Gamond*, 1990).

Internal deformation of calcite crystals within the veins varies from heavily deformed grains to almost undeformed grains. The oldest veins are most strongly deformed, however local variations within one vein generation are also observed and may suggest that stress was heterogeneous on the sample scale.

The most strongly deformed veins are observed in samples S2 and S4. Within sample S2, the veins form irregularly oriented arrays with a vein thickness between < 20 μm and ≈ 200 μm (Figs. 4a, 1b). They are composed of blocky calcite cements that are strongly twinned (Fig. 4b). The twinned crystals display one, two or three sets of straight or weakly bent twins, where bending may indicate the activity of dislocation slip (e.g., *Burkhard*, 1993). Well matching vein boundaries suggest that these veins may have formed as tensile fractures. *Boullier et al.* (2009) described similar veins in drilled core samples of the Chelungpu thrust fault. Up to 3 mm thick vein patches occur in sample S4, composed of large (≈ 1 mm) blocky calcite crystals and sutured boundaries between vein and host rock (Fig. 4c), reminiscent of stylolites. Twins, microfractures and pressure solution seams are observed in large calcite grains where intense twinning is the dominant deformation mechanism (Fig. 4d). The twin densities measured in these strongly deformed calcite grains varies between 82 and 277 twins/mm with a mean density of 135 ± 41 twins/mm and 165 ± 57 twins/mm for samples S2 and S4, respectively (Table 1). None of the calcite grains show evidence of dynamic recrystallization. Calcite veins showing minor deformation are also observed in samples S2, S3, and S4. In sample S2 veins are thin (≤ 50 μm wide) containing coarse-grained calcite that is only moderately deformed (Fig. 4e). A small fraction of the calcite grains are twinned, dominantly showing a single twin set with straight and thin twin lamellae. Irregularly shaped veins occur in samples S3 and S4 (Fig. 4f). The twinned crystals display one or two sets of straight twins. The calcite twin density in sample S2 varies between 14 and 113 twins/mm with a mean density of 56 ± 40 twins/mm. For sample S3 the average density is 93 ± 37 twins/mm (ranging from 11 to 188 twins/mm) and for sample S4 it is 80 ± 27 twins/mm (47-107 twins/mm).

In samples S1 and S2 we found undeformed or only slightly deformed veins crosscutting older and more deformed veins. Veins in sample S2 are straight and range in thickness from 0.7 to 1 mm. They are filled with elongated to fibrous calcites (Fig. 4g). This habit has previously been interpreted to indicate a slow opening during creep (*Gratier and Gamond*, 1990). Very few crystals are fractured or twinned, indicating late cementation processes. The twin density varies between 0 and 65 twins/mm with an average of 22 ± 21 twins/mm. In sample S1 the calcite veins are straight dominated by a twin set with straight and thin twin lamellae. Only a small fraction of the calcite grains is twinned (Fig. 4h). Twin densities in the calcite grains vary between 10 and 63 twins/mm with an average of 27±14 twins/mm (Table 1).

5.2. TEM microstructures and dislocation densities

TEM observations of calcite microstructures were performed on 4 different foils, two from strongly deformed calcite veins of samples S2 and S4 and two from weakly deformed calcite in samples S1 and S2.

Strongly deformed vein cements show evidence for intense intracrystalline plasticity of calcite. Within sample S4 many straight and gently curved dislocations are present, indicating active dislocation glide. Twins are commonly decorated with dislocations (Fig. 5a, left side). A high dislocation density is also present in strongly deformed calcite veins of sample S2 (Fig. 5b). The densities are spatially variable, sometimes forming cell-like networks. Evidence for subgrain formation (dislocation walls) and recrystallization was not detected. The average dislocation density in the strongly deformed calcite veins of sample S4 is $(1.1 \pm 0.5) \times 10^{13}$ m^{-2} and of sample S2 about $(2.7 \pm 1.3) \times 10^{13}$ m^{-2} (Table 1).

In comparison, the weakly deformed calcite grains in sample S1 (Fig. 5c) and sample S2 (Fig. 5d) contain fewer dislocations. The dislocations appear to be straighter than in veins with high dislocation densities. Dislocation densities in samples S1 and S2 are on average $(2.9 \pm 1.1) \times 10^{12}$ m^{-2} and $(3.2 \pm 1.3) \times 10^{12}$ m^{-2}, respectively and about one order of magnitude lower compared to the strongly deformed veins. The scatter of dislocation density measured on a single sample location varies by a factor between ~2 and 3 (Table 1).

5.3. Laue microdiffraction and residual lattice strain

Deformation twinning is observed in the region scanned by the X-ray beam, as shown by maps of *c*-axis orientation in Fig. 6. The xy plane defines the sample surface with the x-direction perpendicular to the X-ray beam incident direction. The calcite in this vein is heavily twinned on a single system. In this map of the orientation angle between the hexagonal crystal *c*-axis and the sample normal (sample z-axis), twin lamellae are observed. Comparing the orientations of the host and twin domain (here host is attributed to the dominant volume and twin to the subordinate volume), it is verified that $e = \{1\bar{1}108\}$ is the twin

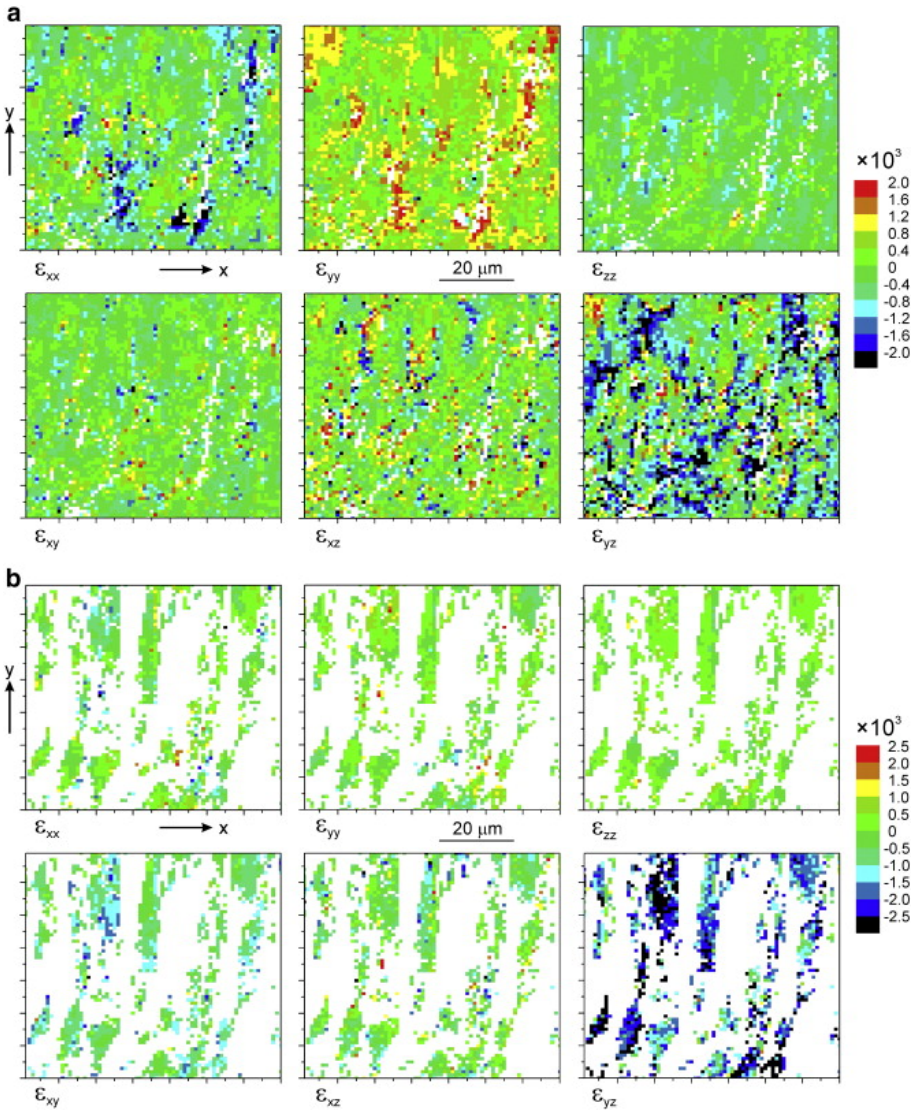

Figure 7. Map of strain components ε_{xx}, ε_{yy}, ε_{zz}, ε_{xy}, ε_{xz}, and ε_{yz} in (a) host domain and (b) twin domain. Units are microstrains. Positive numbers are extension and negative numbers shortening.

plane. The twin plane *e* is inclined 75–80° to the surface of the section (*xy*). Since the twin lamellae are inclined to the sample surface, diffraction patterns recorded with the CCD detector in some regions contain diffraction peaks from both host and twin domains. The two diffraction patterns were separated and individually indexed. Subsequently, the orientation of both grains was grouped and mapped separately. Fig. 6b displays the dominant host with angles 50–54° and Fig. 6c the lamellar twins with angles 73–76°. White spots in the combined orientation map (Fig. 6a) indicate that diffraction pattern taken at these spots could not be indexed. On Fig. 6c we count about 6 twins over the 70 µm scan width. Correcting for 10–15° tilt of the twin planes, this results in a twin density of ≈ 100 twins/mm, which is in excellent agreement with optical measurements. The width of twins is about 5 µm. Based on the number of indexed patterns we estimate a volume fraction of twin:host of 1:5. Determination of the elastic strain tensor was not trivial because of considerable plastic deformation, resulting in distortion of diffraction spots and asterism (Fig. 2b). Distributions of the six strain tensor components are displayed as maps of microstrains in Fig. 7a for host and Fig. 7b for twins. Positive numbers indicate extension and negative numbers compression. The magnitude of lattice strains ranges from 0.8×10^{-3} to 2.2×10^{-3} in the host domains and 1.7×10^{-3} to 3.4×10^{-3} in the twin domains. From the strain maps, it is evident that the components (ε_{yz}) are very large (in compression). This has been previously observed and has been identified as an artifact of the Laue technique in reflection geometry, where this component is extremely sensitive to sample height alignment (*Chen et al.*, 2011). We disregard this component in our interpretation.

6. Discussion

Analysis of the four SAFOD gouge samples revealed a rather complex microstructure with evidence for intense cataclastic deformation, activity of solution–precipitation creep processes, high microporosity, and lubricating amorphous phases (*Janssen et al.*, 2010, 2011). Based on the analysis of dislocation and twin densities of calcite grains within the veins, we can estimate the flow stress in gouge samples using paleo-piezometric relationships. We are using the dislocation density piezometer calibrated by *De Bresser* (1996) on calcite single crystals:

$$\Delta\sigma = 10^{-6.21\pm0.86}\rho_{disloc}^{0.62\pm0.07} \quad (1)$$

where the differential stress $\Delta\sigma$ is given in MPa and dislocation density ρ_{disloc} in m^{-2}. The resulting average stresses vary between 33 and 132 MPa, scattering by about 10 to 90 MPa for a single sample location (Table 1, Fig. 8). However, experimental calibration of the dislocation density piezometer was performed

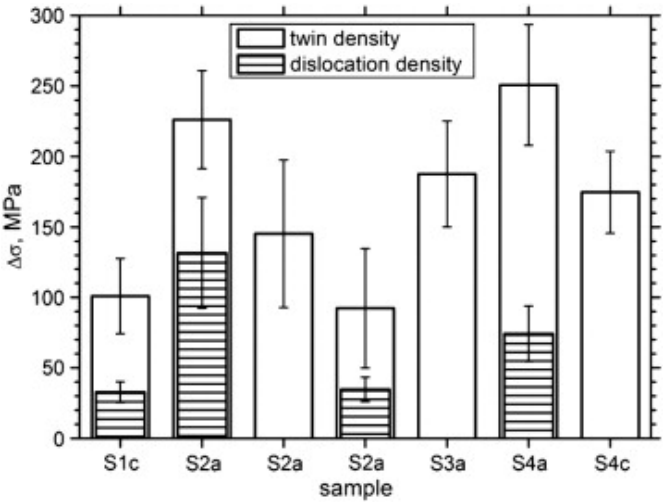

Figure 9. Estimated differential stresses based on paleo-piezometry of measured twin densities (open bars) and dislocation densities (hatched bars) in calcite veins. See text for discussion.

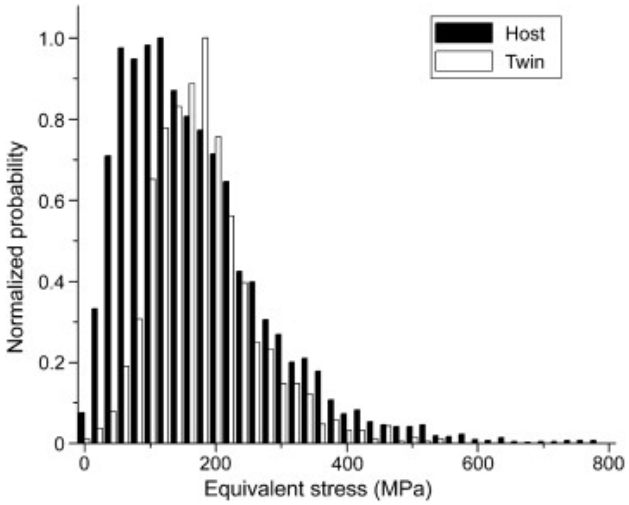

Figure 9. Equivalent stress histogram in host and primary twin domain based on equivalent strain determination. Both host and twin are separately normalized.

by *De Bresser* (1996) at strains > 2%, strain rates of 3×10^{-4} – 3×10^{-8} s^{-1} and temperatures between 550 °C and 800 °C, activating mainly the low temperature r-slip and the high temperature f-slip system. The application of the piezometer generally assumes steady state flow in the dislocation creep regime. It is questionable whether steady state dislocation creep was achieved assuming deformation at the current sampling depth of ~2530–2620 m at temperatures of ~110–115°C (*Williams et al.*, 2004, 2006), although in natural calcite veins intense intracrystalline plasticity was observed at temperatures as low as 150-200°C (*Kennedy and White*, 2001), in greenschist facies rocks (dislocation densities $>10^{15}$ m^{-2}) and limestones subjected to meteorite impact (*Barber and Wenk*, 1976), as well as experimentally deformed limestones at 200 °C (*Barber and Wenk*, 1973). For a temperature of 110°C the critical resolved shear stress for activation of the easiest low temperature (r-) slip system was estimated experimentally to ≈ 80 MPa, corresponding to differential stresses of > 160 MPa assuming a Schmid factor < 0.5 (*De Bresser and Spiers*, 1997). Therefore, the differential stress estimate of < 132 MPa for the SAFOD samples based on dislocation density might be biased by the presence of dislocations associated with twinning (e.g., *Barber and Wenk*, 1979; *Motohashi et al.*, 1976). *De Bresser* (1996) also found that application of the piezometer calibrated experimentally for single crystals to polycrystalline calcite below about 40 MPa flow stress provides an upper bound stress estimate.

A complementary method to estimate paleo-stress is based on the density of calcite twins, since at low temperatures (< 300°C) mechanical e-twinning is an important deformation mechanism in calcite rocks (*Barber and Wenk*, 1979). Paleopiezometers based on twinning in calcite were developed by *Jamison and Spang* (1976) and *Rowe and Rutter* (1990). However, experimental calibration of these piezometers may not be suitable for application to naturally deformed rocks (*Blenkinsop*, 2000; *Burkhard*, 1993; *Ferrill*, 1998; *Rybacki et al.*, 2008). Here, we use a new experimentally calibrated twin density piezometer for calcite that was determined by low temperature (20–350°C) triaxial compression and torsion experiments on Carrara marble:

$$\Delta\sigma = 10^{1.29\pm0.02}\rho_{twin}^{0.50\pm0.05} \quad (2)$$

with $\Delta\sigma$ in MPa and ρ_{twin} is number of twins/mm. Details of the methodology used for the experimental calibration of the piezometer are given in Appendix A1. The twin density-stress relationship appears to be independent of strain and also independent of grain size as pointed out by *Rowe and Rutter* (1990). Estimated average stresses of the inspected samples range between 92 and 251 MPa with an individual scatter between 70 and 200 MPa for a single sample location (Table 1, Fig. 8).

Compared to stress estimates from dislocation densities those from twin densities are in a similar range but up to 2.7 ± 0.7 times higher (Fig. 8). This may point at a systematic error of the experimental piezometer calibrations, for example due to a grain size or strain rate effect. However, as pointed out before, both piezometers are based on different deformation mechanism and it seems likely that they do not converge as long

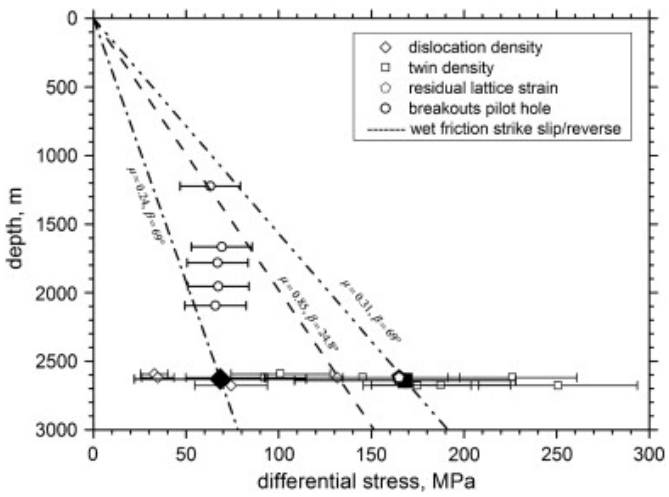

Figure 10. Stress estimates for the SAFOD drill site, California. Microstructure analysis of deformed vein calcite of the main hole shows a wide range of stresses deduced from dislocation and twin densities and residual strain analysis. The large open pentagons represent the stress estimated from residual lattice strain in the host and twin domains of a calcite vein in sample S2. The mean stress value obtained from twin densities (large solid square) corresponds to a weak fault oriented at an angle β of 69° with respect to the maximum horizontal stress direction and a friction coefficient of $\mu = 0.31$. The mean stress calculated from dislocation density (large solid diamond) fits to a friction coefficient of $\mu = 0.24$ and agrees well with stress estimates from borehole breakout measurements (open circles) performed in the pilot hole (*Hickman and Zoback*, 2004). The friction stress for an optimally oriented fault forming an angle β of ≈ 25° between the fault trace and S_H is shown for comparison (broken line) and may represent ancient conditions during formation of the SAF. For calculation of the friction behavior we assumed hydrostatic pore pressure ($\rho_{\text{fluid}} = 1.0$ gcm^{-3}) and a rock density of 2.4 gcm^{-3}.

as temperatures are not high enough to allow steady state high temperature creep of calcite within the veins. In addition, experimental calibration of the dislocation density piezometer was performed by *De Bresser* (1996) at strains > 2% which probably is larger than in the deformed SAFOD samples. During deformation of calcite at low temperature, twinning mostly occurs prior to dislocation slip since the critical resolved shear stress for the activation of twinning is considerably lower than for the main glide systems (*De Bresser and Spiers*, 1997). The dislocations accumulate at twin boundaries where they are pinned (*Barber and Wenk*, 1979). As shown above, pronounced low temperature r-slip and high temperature f-slip, which was mainly observed during experimental calibration of the dislocation density piezometer, is unlikely because of the relatively low temperature at the SAFOD drill site that requires a high CRSS for their activation. We expect therefore that the stress estimate based on dislocation density represents a lower bound, which may explain the difference to the result estimated from twin density. Assuming that no detwinning occurred, the latter is considered to be an upper bound because twinning can be easily activated even at low strain and likely preserves the peak stress conditions. For both used piezometers, the estimated stresses vary quite substantially within the four samples up to a factor of 2.7 (twin density) to 4 (dislocation density) between weakly and strongly deformed vein sections (Table 1). These differences may result from local stress heterogeneity/anisotropy or from different deformation events recorded in the microstructure. However, we were not able to clearly identify and separate chronological vein generations that would support the latter hypothesis. Interestingly, the estimated maximum stresses do not vary systematically with depth or with distance to the active creeping section of the borehole. This may indicate that no strong stress partitioning occurred in the past, although individual stress data vary quite substantially and may be obscured by local strain variations.

A third approach to approximate the local stresses within the calcite veins of the SAFOD samples is to measure the residual microstrain (lattice distortion) preserved in the calcite grains as described above. Lattice strains (Fig. 7) can then be converted to residual stress, by applying Hooke's law $\sigma_i = C_{ij}\varepsilon_j$, where σ_{ij}, C_{ij}, and ε_j are stress tensor (2nd rank), stiffness tensor (4th rank), and strain tensor (2nd rank), respectively. For the elastic tensor of calcite we used experimental values of *Chen et al.* (2001, their abstract). They agree closely with previous measurements (Table 1 in *Chen et al.*, 2001). Statistical information about the magnitude of differential residual stress can be obtained by converting components of the strain tensor to an equivalent stress, defined as follows (*Liu*, 2005):

$$\sigma_{eq} = \sqrt{\frac{(\sigma_{11}-\sigma_{22})^2 + (\sigma_{22}-\sigma_{33})^2 + (\sigma_{33}-\sigma_{11})^2 + 6(\sigma_{12}^2 + \sigma_{13}^2 + \sigma_{23}^2)}{2}} \quad (3)$$

but we set the component σ_{23} (corresponding to ε_{yz}) to zero to exclude artifacts of the technique. This equivalent stress can thus be interpreted as a lower limit. The equivalent stress distribution of host and twin domains is shown in histograms of Fig. 9. The distribution maximum is at 140 MPa and 190 MPa for host and twin domains, respectively, with an average of 165 MPa, and the full width at half maximum of the distribution is about 190 MPa for both host and twin domains (Table 1). The observed stresses in SAFOD vein calcite are higher than stresses associated with twins in recrystallized greens-chist facies marble where average values of 60-70 MPa and 110 MPa in host and twin domains, respectively, were observed (*Chen et al.*, 2011). Stress estimate from twin density of about 100 twins/mm in the examined sample section gives a differential stress of ≈ 195 MPa, which is in good agreement with values obtained from the preserved lattice distortion. The measured elastic lattice distortion likely represents the preserved local yield stress and twinning mimics the inelastic stress at a somewhat higher strain. The two techniques result in stress estimates that are not significantly different, but higher than the stress estimate based on dislocation densities.

Assuming that the results of the microstructure analysis constrain approximately the paleo-stresses sustained by the collected SAFOD samples, we may compare our results with in-situ stress measurements and theoretical bounds for friction-dominated fault stresses (Fig. 10). The in-situ stress estimates are adopted from borehole breakout measurements performed by *Hickman and Zoback* (2004) in the 2.2 km-deep SAFOD pilot hole. The authors obtained a general increase in the angle between the SAF trace and the maximum horizontal stress S_H up to about 69 ± 14° at 2050-2200 m depth, but with some localized stress rotations close to active faults. Estimated stresses show a transpressional regime with a magnitude of S_H being about twice as high as the minimum horizontal stress S_h, which itself is approximately equal to the overburden stress S_v. The inferred differential stress $\Delta\sigma$ ($\approx S_H - S_h \approx S_H - S_v$) is nearly constant about 60-70 MPa in a depth range of 1223-2095 m (Fig. 10). Extrapolation of these results to the depth (≈ 2.6 km) of samples S1-S4 from the main hole are in good agreement to the average stress determined from dislocation densities (68 ± 46 MPa), but about 2.5 times lower than the average stress of 168 ± 60 MPa and 165 MPa estimated from twin densities and residual strain analysis, respectively (Fig. 10). The discrepancies may be explained by the uncertainties associated with the different techniques and particularly the local concentration of stress. Even single phase polycrystalline calcite shows locally high strain (and associated stress) heterogeneities when deformed in dislocation creep (*Xu and Evans*, 2010). For deformation of polyphase rocks the local stress may vary substantially between different phases, depending on composition, geometry, and boundary conditions (e.g., *Kenkmann and Dresen*, 1998; *Kenkmann*, 2000; *Ji et al.*, 2000; *Holyoke and Tullis*, 2006). In addition, borehole breakout measurements represent the recent borehole-scale stress field, whereas preserved microstructures likely represent the maxi-mum local (grain-) scale paleo-stresses sustained by the samples. It is also possible that twinning was produced by localized high transient stresses during seismic events (similar to the knife-edge experiment of *Baumhauer*, 1879), while dislocation structures formed during steady-state creep. This would be analogous to Dauphiné twinning in quartz (*Schubnikov* 1930). Strikingly the stress estimates based on entirely different techniques involving different scales of observation show a very reasonable agreement.

At the SAFOD site the dip of the SAF is close to vertical (≈ 83°) and the angle β between the trace of the fault and the maximum horizontal stress is about 69° in the depth considered here (*Hickman and Zoback*, 2004; *Zoback et al.*, 2010). Assuming that one principal stress direction is vertical (Andersonian faulting) and that the inter-mediate principal stress $\sigma_2 = S_h \approx S_V$ (*Hickman and Zoback*, 2004), then the differential stress for strike slip faulting can be calculated using the following equation

$$\Delta\sigma = \frac{\tau_0 + \mu(S_V - P_0)}{\sin(\beta)\,\cos(\beta) - \mu\sin^2(\beta)} \quad (4)$$

(see Appendix A2). P_0 is pore pressure, τ_0 is the cohesion, and μ is the friction coefficient.

According to Byerlee' rule for friction of rocks $\tau_0 = 0$, $\mu = 0.85$ for effective normal stresses on the fault < 200 MPa and $\tau_0 = 50$ MPa, $\mu = 0.6$ otherwise (*Byerlee*, 1978). At given friction coefficient, the optimum orientation of the fault that requires the minimum stress to be activated is given by

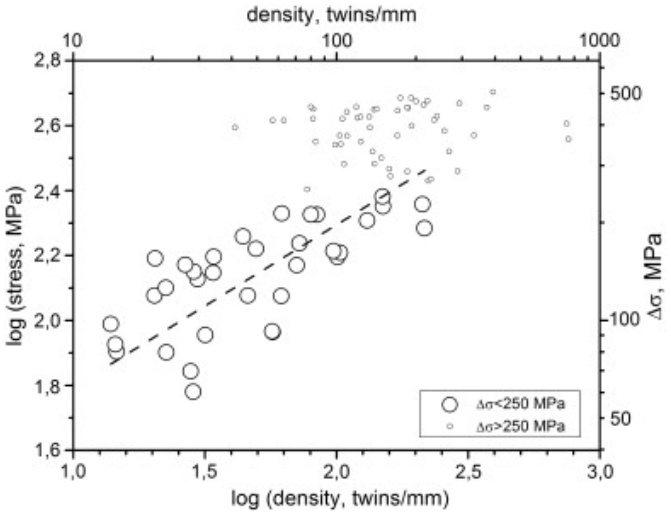

Figure 11. Log-log plot of twin line density vs. differential stress measured in experimentally deformed Carrara marble at temperatures of 20°C-350°C, confining pressure of 300-400 MPa, and a strain rate of $\sim 10^{-4}$ s^{-1}. Best fit regression for data b250 MPa (large symbols) yields a slope of 0.50 ± 0.05 and an intersection of 1.29 ± 0.02.

$\mu = -1/\tan(2\beta)$ (*Jaeger and Cook*, 1969). For $\mu = 0.85$, $\tau_0 = 0$ and assuming hydrostatic pore pressure, the resulting differential stress for an optimally oriented fault is in between the values obtained from dislocation and twin density measurements (broken line in Fig. 10). However, for this case the corresponding angle β between S_H and the trace of the SAF should be ≈ 25°, which is not fulfilled. Taking instead the measured value of $\beta \approx 69°$, requires friction coefficients of $\mu \approx 0.24$ to $\mu \approx 0.31$ to fit to the stress estimates from dislocation density and twin density, respectively (dotted-broken lines in Fig. 10). A low maximum friction coefficient of $\mu \approx 0.2$ has also been inferred earlier for the San Andreas Fault based on observations of heat flow and stress orientation (e.g., *Hickman*, 1991). Therefore, under the premise that our results from microstructure analysis constrain the (paleo-) stress at the SAFOD site, the SAF appears to be a weak fault (*Hickman and Zoback*, 2004). Elevated pore pressure can also reduce the effective differential stress on an unfavorably oriented fault, but whether pore fluid pressure in the SAF is high or not is still a matter of debate (*Gratier et al.*, 2009; *Holdsworth et al.*, 2009; *Janssen et al.*, 2011; *Zoback et al.*, 2010). The estimated friction coefficients between $\mu \approx 0.24$ and $\mu \approx 0.31$ agree well with the presence of low-friction minerals as for example clays, talc or serpentine (e.g., *Carpenter et al.*, 2009; *Carpenter et al.*, 2011; *Collettini et al.*, 2009; *Moore and Rymer*, 2007; *Tembe et al.*, 2009) but may be also influenced by amorphous phases found in the fault gouge (*Janssen et al.*, 2010).

By use of Eq. A3 (Appendix A2) it can be shown that these friction coefficients are hardly influenced by the actual dip ($\gamma \approx 83°$) of the SAF (resulting in an increase of $\mu < 1\%$), by a slight non-zero rake (increase of $\mu = 5\%$ for $\lambda = 10°$), or by a 50%-increase of the pore pressure (increase of $\mu < 8\%$). However, the friction coefficient can easily exceed values of $\mu = 0.6$ if the intermediate principal stress S_V is distinctly higher than the minimum horizontal stress S_h ($\delta \geq 0.5$ in Eq. A3), which appears to be the typical case along the SAF (*Provost and Houston*, 2003). Therefore, the estimated friction coefficients may be regarded as lower limits owing to the assumed magnitude of S_V to be close to S_h as determined from the borehole breakout measurements in the pilot hole (*Hickman and Zoback*, 2004).

Considering that the samples were collected close to the southwest and central deforming zones, we may also estimate the stress at depth by applying laboratory derived flow laws for creep of rocks. Assuming a temperature of 110°C in 2.6 km depth, a creep strain rate of 10^{-12} s^{-1} and a grain size d of 10 μm for grain size sensitive creep behavior, the predicted stress for dislocation creep of calcite is $\sim 3 \times 10^5$ MPa (*Schmid et al.*, 1980), for grain boundary diffusion/sliding $\sim 3 \times 10^6$ MPa (*Herwegh et al.*, 2005), and for grain boundary sliding accommodated by dislocation activity and volume diffusion $\sim 9 \times 10^3$ MPa (*Walker et al.*, 1990). These values are far too high to represent realistic stresses. If we assume that the stress state is governed by creep deformation of phyllosilicates like clays, serpentinite, or micas, reliable flow laws are scarce so far. *Kronenberg et al.* (1990) measured basal slip of biotite single crystals for which the extrapolated creep law yields a stress of ~25 MPa and the flow law for biotite schist obtained by *Shea and Kronenberg* (1992) yields ~160 MPa differential stress, both of which are in agreement with the range of stresses estimated from our microstructural observations. Applying the flow laws derived by *Paterson* (1995) for solution precipitation creep of porous quartz (5% porosity) yields a stress of ~1700 MPa for $d = 10$ μm to ~100 MPa for $d = 1$ μm, if controlled by the rate of diffusion within islands at the grain interface (source/sink diffusion control). Clearly, more reliable creep laws are required to better constrain the stress of the creeping portion of the SAF.

Acknowledgments

We thank Stefan Gehrmann for thin section preparation, Anja Schreiber for TEM foil preparation, David Seydewitz for counting dislocation densities, and Manuel Kienast for discussions. Access to beamline 12.3.2. at ALS and help from Martin Kunz is gratefully acknowledged, as well as the SAFOD science team for providing samples. CJ was partly funded by DFG grant JA 573/4-1. HRW is appreciative for support through NSFEAR-0836402 and DOE. We are also thankful for the thoughtful reviews of Marco Herwegh and an anonymous reviewer.

Appendix

A1. Twin density piezometer

In the following we briefly summarize the experimental methods used to establish a piezometer based on twin densities within deformed calcite marble (cf., *Rybacki et al.*, 2008). Triaxial compression and torsion experiments were performed on 14 cylindrical Carrara marble samples in the semibrittle regime at temperatures of 20°C-350°C, 300-400 MPa confining pressure, and strain rates of $\sim 10^{-4}$ s^{-1} in a Paterson-type deformation apparatus. Maximum axial strain was about 12% and maximum shear strain < 1.7. The density of twins was measured with an optical microscope in different positions on polished thin sections, oriented either parallel or perpendicular to the sample axis. The twin (line) density was determined by counting the number of twins within a grain divided by the grain diameter in the direction perpendicular to the twin boundaries and normalized to 1 mm length. For grains containing more than one twin set this procedure was repeated for each orientation and the average value calculated. Measurements were restricted to thick (> 1 μm), optically visible twins up to line densities < 500-700 twins/mm, above which they are hard to distinguish because of the extremely fine spacing. In axially compressed samples the measured stress and strain is homogeneously distributed and in twisted samples the shear stress and strain at each position was calculated from geometrical considerations (*Paterson and Olgaard*, 2000). In total we determined the twin density ρ twin and corresponding stress $\Delta\sigma$ and strain at 95 positions within the deformed samples, where the reported twin density at each position represents an average of 4-6 measurements. The result is shown in Fig. A1 in a log-log diagram. Linear regression of the form $\log(\Delta\sigma) = \sigma_0 + m \cdot \log \rho_{twin}$ yields the constants $\sigma_0 =$

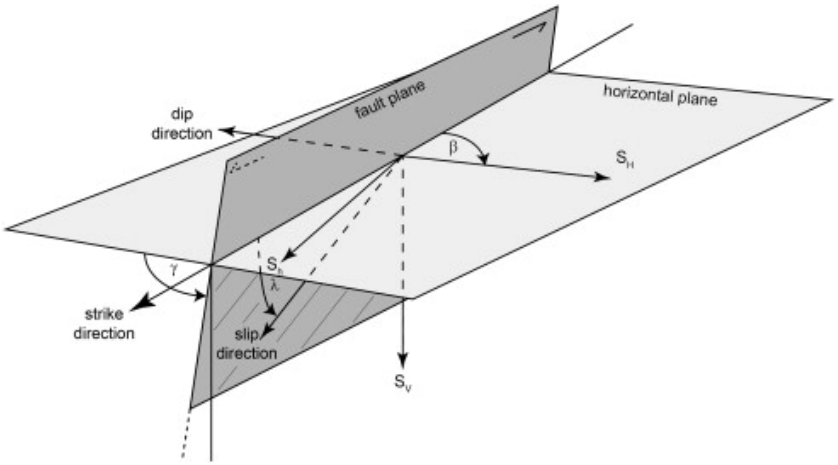

Figure 12. Schematic drawing showing the definition of angles β, γ, and λ used to describe the relative orientation of a fault plane relative to the principal stress directions S_H, S_h, and S_V. The strike direction is defined along the line of strike such that the dip direction is to the right. For downward slip direction (with respect to the horizontal plane) the rake λ is < 180° and for upward slipping 180° < λ < 360°.

1.29 ± 0.02 and $m = 0.50 \pm 0.05$ when restricting the stress to less than about 250 MPa that may be a realistic geologically relevant stress range (broken line in Fig. A1). Taking all data up to 510 MPa differential stress (small symbols) into account would increase the estimated stress by about 25%. Few measurements of the dislocation density within deformed samples indicate that the stress predicted by the twin and dislocation density piezometer agrees very well, if the applied stress is above the CRSS for low temperature dislocation glide of calcite.

A2. Friction on planar faults

Following *Jaeger and Cook* (1969) and *Zoback* (2007) the stress acting on an arbitrary oriented fault may be derived from a stress tensor transformation of the form $\sigma = A \cdot S \cdot A^T$, where σ is the stress tensor in the fault system with Cartesian coordinates defined by x in the slip direction in the fault plane, y perpendicular to the fault plane, and z perpendicular to both x and y. S is the effective stress tensor with the non-zero principal stress components $S_{11} = S_H - P_0$, $S_{22} = S_h - P_0$, and $S_{33} = S_V - P_0$, where S_H and S_h are the maximum and minimum horizontal stress, respectively, S_V is the vertical stress (overburden), and P_0 is pore pressure. Defining the relative orientation of the fault with respect to the principal stress tensor by three angles (Fig. A2), β = angle between fault strike direction and S_H measured clockwise, γ = fault dip measured from horizontal clockwise when looking in fault strike direction, and λ = fault rake, i.e. the angle between fault strike direction and slip direction in the fault plane, allows to set up the transformation matrix A by three successive rotations of the principal stress coordinate system, which is given by:

$$A = \begin{pmatrix} a_{11} & a_{12} & a_{13} \\ a_{21} & a_{22} & a_{23} \\ a_{31} & a_{32} & a_{33} \end{pmatrix}$$

with the direction cosines

a_{11} $\cos(\beta)\cos(\lambda) + \sin(\beta)\cos(\gamma)\sin(\lambda)$,
a_{12} $-\sin(\beta)\cos(\lambda) + \cos(\beta)\cos(\gamma)\sin(\lambda)$,
a_{13} $\sin(\gamma)\sin(\lambda)$,
a_{21} $\sin(\beta)\sin(\gamma)$,
a_{22} $\cos(\beta)\sin(\gamma)$,
a_{23} $-\cos(\gamma)$,
a_{31} $-\cos(\beta)\sin(\lambda) + \sin(\beta)\cos(\gamma)\cos(\lambda)$,
a_{32} $\sin(\beta)\sin(\lambda) + \cos(\beta)\cos(\gamma)\cos(\lambda)$, and
a_{33} $\sin(\gamma)\cos(\lambda)$.

Friction (or Coulomb failure) along the fault is given by $\tau = \tau_0 + \mu \cdot \sigma_n$ (e.g., *Jaeger and Cook*, 1969), where $\tau = \sigma_{21}$ is the shear stress in slip direction, $\sigma_n = \sigma_{22}$ is the normal stress perpendicular to the fault, τ_0 is cohesion, and μ is the friction coefficient. Combining the friction criterion and the stress transformation equations allows calculating the differential stress $\Delta\sigma$ for the three different cases of thrust faulting, normal faulting, and strike slip, taking into account the magnitude of the intermediate principal stress:

1) Thrust faulting: $\Delta\sigma_{TF} = (S_H - S_V)$ with $S_H \geq S_h \geq S_V$ and $S_h = S_V + \delta \cdot \Delta\sigma, 0 \leq \delta \leq 1$

$$\Delta\sigma_{TF} = \frac{\tau_0 + \mu(S_V - P_0)}{(a_{11}a_{21} + a_{12}a_{22}\delta) - \mu(a_{21}^2 + a_{22}^2\delta)} \quad \text{(A1)}$$

2) Normal faulting: $\Delta\sigma_{NF} = (S_V - S_h)$ with $S_V \geq S_H \geq S_h$ and $S_H = S_h + \delta \cdot \Delta\sigma, 0 \leq \delta \leq 1$

$$\Delta\sigma_{NF} = \frac{\tau_0 + \mu(S_V - P_0)}{(a_{13}a_{23} + a_{11}a_{21}\delta) - \mu(a_{23}^2 + a_{21}^2\delta) + \mu} \quad \text{(A2)}$$

3) Strike slip: $\Delta\sigma_{SS} = (S_H - S_h)$ with $S_H \geq S_V \geq S_h$ and $S_V = S_h + \delta \cdot \Delta\sigma, 0 \leq \delta \leq 1$

$$\Delta\sigma_{SS} = \frac{\tau_0 + \mu(S_V - P_0)}{(a_{11}a_{21} + a_{13}a_{23}\delta) - \mu(a_{21}^2 + a_{23}^2\delta) + \mu \cdot \delta} \quad \text{(A3)}$$

For a vertical strike slip fault (γ =90°) slipping in horizontal direction (λ = 0°), the last equation can be simplified to

$$\Delta\sigma = \frac{\tau_0 + \mu(S_V - P_0)}{\sin(\beta)\cos(\beta) - \mu\sin^2(\beta) + \mu \cdot \delta} \quad \text{(A4)}$$

that equals Eq. (4) for $\delta = 0$, i.e. $S_V = S_h$.

References

Barber, D.J., Wenk, H.R., 1973. The microstructure of experimentally deformed limestones. J. Mat. Sci. 8, 500–508.
Barber, D.J., Wenk, H.R., 1976. Defects in deformed calcite and carbonate rocks. In: Wenk, H.R. (Ed.), Electron Microscopy in Mineralogy. Springer, Berlin, pp. 428–442.
Barber, D.J., Wenk, H.R., 1979. Deformation twinning in calcite, dolomite,

and other rhombohedral carbonates. Phys. Chem. Min. 5, 141–165.
Baumhauer, H., 1879. Ueber kuenstliche Kalkspath-Zwillinge nach −1/2 R. Zeitschrift Krystallogr 3, 588–591.
Blenkinsop, T., 2000. Deformation microstructures and mechanisms in minerals and rocks. Kluwer Academic Publishers, London.
Boullier, A.M., Yeh, E.C., Boutareaud, S., Song, S.R., Tsai, C.H., 2009. Microscale anatomy of the 1999 Chi-chi earthquake fault zone. Geochem. Geophys. Geosystems 10, Q03016.
Bradbury, K.K., Barton, D.C., Solum, J.G., Draper, S.D., Evans, J.P., 2007. Mineralogical and textural analyses of drill cuttings from the San Andreas Fault Observatory at Depth (SAFOD) boreholes: initial interpretations of fault zone composition and constraints on geological models. Geosphere 3, 299–318.
Brodsky, E.E., Mori, J., Fulton, P.M., 2010. Drilling into faults quickly after earthquakes. EOS Trans. AGU 91 (27), 237–238.
Brune, J.N.T., Henyey, T., Roy, R., 1969. Heat flow, stress, and rate of slip along the San Andreas Fault, California. J. Geophys. Res. 74, 3821–3827.
Burkhard, M., 1993. Calcite twins, their geometry, appearance and significance as stress–strain markers and indicators of tectonic regime: a review. J. Struct. Geol. 15 (3–5), 351–368.
Byerlee, J., 1978. Friction of rocks. Pure Appl. Geophys. 116, 615–626.
Carpenter, B.M., Marone, C., Saffer, D.M., 2009. Frictional behavior of materials in the 3D SAFOD volume. Geophys. Res. Lett. 36, L05302. doi: 10.1029/2008GL036660.
Carpenter, B.M., Marone, C., Saffer, D.M., 2011. Weakness of the San Andreas Fault revealed by samples from the active fault zone. Nature Geosci. 4 (4), 251–254.
Chéry, J., Zoback, M.D., Hickman, S., 2004. A mechanical model of the San Andreas Fault and SAFOD Pilot Hole stress measurements. Geophys. Res. Lett. 31, L15S13. doi: 10.1029/2004GL019521.
Chen, C.C., Lin, C.C., Liu, L.G., Sinogeikin, S.V., Bass, J.D., 2001. Elasticity of single-crystal calcite and rhodochrosite by Brillouin spectroscopy. Am. Mineral. 86 (11–12), 1525–1529.
Chen, K., Kunz, M., Tamura, N., Wenk, H.-R., 2011. Deformation twinning and residual stress in calcite studied with synchrotron polychromatic X-ray microdiffraction. Phys. Chem. Minerals 38 (6), 491–500.
Chester, F.M., Logan, L.M., 1986. Implication for mechanical properties of brittle faults from observations of Punchbowl fault zone, California. Pure Appl. Geophys 124, 79–106.
Collettini, C., Niemeijer, A., Viti, C., Marone, C., 2009. Fault zone fabric and fault weakness. Nature 462, 907–910.
De Bresser, J.H.P., 1996. Steady state dislocation densities in experimentally deformed calcite materials: single crystals versus polycrystals. J. Geophys. Res. 101 (B10), 22189–22201.
De Bresser, J.H.P., Spiers, C.J., 1997. Strength characteristics of the r, f, and c slip systems in calcite. Tectonophys. 272 (1), 1–23.
Ebert, A., Herwegh, M., Pfiffner, A., 2007. Cooling induced strain localization in carbonate mylonites within a large-scale shear zone (Glarus thrust, Switzerland). J. Struct. Geol. 29, 1164–1184.
Evans, J.P., Chester, F.M., 1995. Fluid–rock interaction in faults of the San Andreas system: inferences from San Gabriel fault rock geochemistry. J. Geophys. Res. 100, 13007–13020.
Fagereng, A., Remitti, F., Sibson, R.H., 2010. Shear veins observed within anisotropic fabric at high angles to the maximum compressive stress. Nature Geosci. 3 (7), 482–485.
Faulkner, D.R., Mitchell, T.M., Healy, D., Heap, M.J., 2006. Slip on 'weak' faults by the rotation of regional stress in the fracture damage zone. Nature 444, 922–925.
Ferrill, D.A., 1998. Critical re-evaluation of differential stress estimates from calcite twins in coarse-grained limestone. Tectonophys. 285 (1–2), 77–86.
Fulton, P.M., Saffer, D.M., Bekins, B.A., 2009. A critical evaluation of crustal dehydration as the cause of an overpressured and weak San Andreas Fault. Earth Planet. Sci. Lett. 284, 447–454.
Graf, D.L., 1961. Crystallographic tables for the rhombohedral carbonates. Am. Mineral. 46 (11–2), 1283–1316.
Gratier, J.P., Gamond, J.F., 1990. Transition between seismic and aseismic deformation in the upper crust. Geol. Soc. Spec. Publ. 54, 461–473.
Gratier, J.P., Favreau, P., Renard, F., 2003. Modeling fluid transfer along California faults when integrating pressure solution crack sealing and compaction processes. J. Geophys. Res. 108 (B2), 2104.
Gratier, J.P., Richard, J., Mittempergher, S., Renard, F., Doan, M., Di Toro, G., Hadizadeh, J., Boullier-Betrand, A., 2009. Pressure solution as a mechanism of creep and sealing in active faults: evidence from the SAFOD samples. EOS Trans. AGU 90 (52) Fall Meet. Suppl., Abstr. T21B-1795.
Ham, R.K., 1961. The determination of dislocation densities in thin films. Phil. Mag. 6 (69), 183–1184.
Ham, R.K., Sharpe, N.G., 1961. A systematic error in the determination of dislocation densities in thin films. Phil. Mag. 6 (69), 1193–1194.
Hardebeck, J.L., Michael, A.J., 2004. Stress orientations at intermediate angles to the San Andreas Fault, California. J. Geophys. Res. 109, B11303 11310.11029/12004JB003239.
Herwegh, M., Kunze, K., 2002. The influence of nano-scale second-phase particles on deformation of fine-grained calcite mylonites. J. Struct. Geol. 24, 1463–1478.
Herwegh, M., De Bresser, J.H.P., ter Heege, J.H., 2005. Combining natural microstructures with composite flow laws: an improved approach for the extrapolation of lab data to nature. J. Struct. Geol. 27 (3), 503–521.
Hickman, S., 1991. Stress in the lithosphere and the strength of active faults, U.S. Nat. Rep. Int. Union Geod. Geophys. 1987–1990. Rev. Geophys. 29, 759–775.
Hickman, S., Zoback, M.D., 2004. Stress orientations and magnitudes in the SAFOD pilot hole. Geophys. Res. Lett. 31, L15S12.
Hickman, S., Zoback, M.D., Ellsworth, W., Chester, J., Chester, F., Evans, J., Moore, D., Kirschner, D., Schleicher, A., van der Pluijm, B.A., Solum, J., 2008. Structure and composition of the San Andreas Fault in central California: recent results from SAFOD sample analyses. EOS Trans. AGU, 89. Fall Meet. Suppl., Abstr. T53F-01.
Holdsworth, R.E., van Diggeln, E., Spiers, C., De Bresser, H.J., Smith, S.A., 2009. The microstructural character and evolution of fault rocks from the SAFOD core and potential weakening mechanisms along the San Andreas Fault. EOS Trans. AGU 90 (52) Fall Meet. Suppl., Abstract T52B-01.
Holyoke III, C.W., Tullis, J., 2006. Mechanisms of weak phase interconnection and the effects of phase strength contrast on fabric development. J. Struct. Geol. 28 (4), 621–640.
Jaeger, J., Cook, N., 1969. Fundamentals of Rock Mechanics. Chapman and Hall, London.
Jamison, W.R., Spang, J.H., 1976. Use of calcite twin lamellae to infer differential stress. Geol. Soc. Am Bull. 87 (6), 868–872.
Janssen, C., Laube, N., Bau, M., Fray, D.R., 1998. Fluid regime in faulting deformation of the Waratah Fault Zone, Australia, as inferred from major and minor element analyses and stable isotopic signatures. Tectonophys. 294, 109–130.
Janssen, C., Wirth, R., Rybacki, E., Naumann, R., Kemnitz, H., Wenk, H.-R., Dresen, G., 2010. Amorphous material in SAFOD core samples (San Andreas Fault): evidence for crush-origin pseudotachylytes? Geophys. Res. Lett. 37, L01303.
Janssen, C., Wirth, R., Reinicke, A., Rybacki, E., Naumann, R., Wenk, H.-R., Dresen, G., 2011. Nanoscale porosity in SAFOD core samples (San Andreas Fault). Earth Planet. Sci. 301, 179–189.
Ji, S., Wirth, R., Rybacki, E., Jiang, Z., 2000. High-temperature plastic deformation of quartz-plagioclase multilayers by layer-normal compression. J. Geophys. Res. 105 (B7), 16651–16664.
Kenkmann, T., 2000. Processes controlling the shrinkage of porphyroclasts in gabbroic shear zones. J. Struct. Geol. 22 (4), 471–487.
Kenkmann, T., Dresen, G., 1998. Stress gradients around porphyroclasts palaeopiezo-metric estimates and numerical modeling. J. Struct. Geol. 20 (2–3), 163–173.
Kennedy, L.A., White, J.C., 2001. Low-temperature recrystallization in calcite: mechanisms and consequences. Geology 29 (11), 1027–1030.
Kronenberg, A.K., Kirby, S.H., Pinkston, J., 1990. Basal slip and mechanical anisotropy of biotite. J. Geophys. Res. 95, 19257–19278.
Kunz, M., Tamura, N., Chen, K., MacDowell, A.A., Celestre, R.S., Church, M.M., Fakra, S., Domning, E.E., Glossinger, J.M., Kirschman, J.L., Morrison1, G.Y., Plate, D.W., Smith, B.V., Warwick, T., Yashchuk, V.V., Padmore, H.A., Ustundag, E., 2009. A dedicated superbend X-ray microdiffraction beamline for materials, geo-, and environmental sciences at the advanced light source. Rev. Sci. Instrum. 80, 035108.
Lachenbruch, A., Sass, J., 1980. Heat flow and energetics of the San Andreas Fault zone. J. Geophys. Res. 85, 6185–6222.
Lachenbruch, A., Sass, J., 1992. Heat flow from Cajon Pass, fault strength, and tectonic implications. J. Geophys. Res. 97, 4995–5015.
Liu, A.F., 2005. Mechanics and Mechanism of Fracture. ASM International, Schaumburg, Illinois.
Lockner, D.A., Morrow, C., Moore, D., Hickman, S., 2011. Low strength of deep San Andreas Fault gouge from SAFOD core. Nature 472, 82–85.
Mittempergher, S., Di Toro, G., Gratier, J.P., Hadizadeh, J., Smith, S.A.F., Spiess, R., 2011. Evidence of transient increases of fluid pressure in SAFOD phase III cores. Geophys. Res. Lett. 38, L03301. doi: 10.1029/2010GL046129.
Moore, D.E., Rymer, M.J., 2007. Talc-bearing serpentinite and the creep-

ing section of the San Andreas Fault. Nature 448, 795–797.
Motohashi, Y., Braillon, P., Serughetti, J., 1976. Elastic energy, stress field of dislocations, and dislocation parameters in calcite crystals. Phys. Stat. Sol. 37, 263–270.
Paterson, M., 1995. A theory for granular flow accommodated by material transfer via intergranular fluid. Tectonophys. 245, 135–151.
Paterson, M., Olgaard, D.L., 2000. Rock deformation tests to large shear strains in torsion. J. Struct. Geol. 22, 1341–1358.
Pezzotti, G., Kleebe, H.J., 1996. Quantitative characterization of dislocation density in α-SiC crystals after high-pressure sintering in Si3N4 matrix. J. Mater. Sci. Lett. 15 (6), 500–504.
Pollard, D.D., Segall, P., 1987. Theoretical displacements and stresses near fractures in rock with application of faults, joints, veins dikes, and solution surfaces. In: Atkinson, B.K. (Ed.), Fracture Mechanics of Rock. Academic Press, London, pp. 277–349.
Provost, A.-S., Houston, H., 2003. Stress orientations in northern and central California: evidence for the evolution of frictional strength along the San Andreas plate boundary system. J. Geophys. Res. 108 (B3), 2175. doi: 10.1029/2001JB001123.
Rowe, K.J., Rutter, E.H., 1990. Palaeostress estimation using calcite twinning: experimental calibration and application to nature. J. Struct. Geol. 12, 1–17.
Rybacki, E., Janssen, C., Dresen, G., 2008. Stress and temperature dependence of calcite twinning: new experimental and field constraints. EOS Trans. AGU, Fall Meet. Suppl., Abstract T23C-2069.
Schleicher, A.M., Warr, L.N., van der Pluijm, B.A., 2009. On the origin of mixed-layered clay minerals from the San Andreas Fault at 2.5–3 km vertical depth (SAFOD drillhole at Parkfield, California). Contrib. Miner. Petrol. 157, 173–187.
Schmid, S., Paterson, M., Boland, J., 1980. High temperature flow and dynamic recrystallization in Carrara marble. Tectonophys. 65, 245–280.
Schoek, G., 1961. Correlation between dislocation length and density. J. Appl. Phys. 33 (6), 1745–1747.
Scholz, C.H., 2000. Evidence for a strong San Andreas Fault. Geology 28, 163–166.
Scholz, C.H., Hanks, T.C., 2004. The strength of the San Andreas Fault: a discussion. In: Karner, G.D., et al. (Ed.), Rheology and Deformation of the Lithosphere at Continental Margins. Columbia Univ. Press, New York, pp. 261–283.
Schubnikov, A., 1930. Ueber Schlagfiguren des Quarzes. Z. Kristallogr. 74, 103–104.
Schulz, S.E., Evans, J.P., 2000. Mesoscopic structure of the Punchbowl Fault, Southern California and the geological and geophysical structure of active strike-slip faults. J. Struct. Geol. 22, 913–930.
Shea, W.T., Kronenberg, A.K., 1992. Rheology and deformation mechanisms of an isotropic mica schist. J. Geophys. Res. 97, 15201–15237.
Springer, D.S., Evans, J.P., Garver, J.L., Kirschner, D., Janecke, S., 2009. Arkosic rocks from the San Andreas Fault observatory at depth (SAFOD) borehole, central California: implications for structure and tectonics of the San Andreas Fault zone. Lithosphere 1, 206–226.
Tamura, N., Kunz, M., Chen, K., Celestre, R.S., MacDowell, A.A., Warwick, T., 2009. A superbend X-ray microdiffraction beamline at the advanced light source. Mat. Sci. Eng. A 524 (1–2), 28–32.
Tembe, S., Lockner, D., Wong, T.-F., 2009. Constraints on the stress state of the San Andreas Fault with analysis based on core and cuttings from San Andreas Fault Observatory at Depth (SAFOD) drilling phases 1 and 2. J. Geophys. Res. 114, B11401 11410.11029/ 12008JB005883.
Townend, J., Zoback, M.D., 2004. Regional tectonic stress near the San Andreas Fault in central and southern California. Geophys. Res. Lett 31, L15S11.
Walker, A., Rutter, E., Brodie, K., 1990. Experimental study of grain-size sensitive flow of synthetic, hot-pressed calcite rocks. In: Knipe, R.J., Rutter, E.H. (Eds.), Deformation, Mechanisms, Rheology and Tectonics. Geol. Soc. Spec. Publ, London, pp. 259–284.
Williams, C.F., Grubb, F.V., Galanis, S.P., 2004. Heat flow in the SAFOD pilot hole and implications for the strength of the San Andreas Fault. Geophys. Res. Lett. 31. doi: 10.1029/2003GL019352 L15S14.
Williams, C.F., Grubb, F.V., Galanis, S.P., 2006. Heat flow measurements across the San Andreas Fault near Parkfield, California - preliminary results from SAFOD. EOS Trans. AGU 87 (52) Fall Meet. Suppl. Abstract S33B-0241.
Wiltschko, D.V., Lambert, G.R., Lamb, W., 2009. Conditions during syntectonic vein formation in the footwall of Absaroka Thrust Fault, Idaho-Wyoming-Utah fold and thrust belt. J. Struct. Geol. 31, 1039-1057.
Wirth, R., 2004. Focused Ion Beam (FIB): a novel technology for advanced application of micro- and nano-analysis in geosciences and applied mineralogy. Eur. J. Mineral. 16 (6), 863–876.
Wirth, R., 2009. Focused Ion Beam (FIB) combined with SEM and TEM: advanced analytical tools for studies of chemical composition, microstructure and crystal structure in geomaterials on a nanometre scale. Chem. Geol. 261 (3–4), 217–229.
Xu, L., Evans, B., 2010. Strain heterogeneity in deformed Carrara marble using a microscale strain mapping technique. J. Geophys. Res. 115 (B4), B04202. doi: 10.1029/2009jb006458.
Zoback, M.D., 2007. Reservoir Geomechanics. Cambridge Univ. Press, New York.
Zoback, M.D., et al., 1987. New evidence for the state of stress on the San Andreas Fault system. Science 238, 1105–1111.
Zoback, M.D., Hickman, S., Ellsworth, W., 2010. Scientific drilling into the San Andreas Fault zone. EOS Trans. AGU 91 (22), 197–199.